Nationwide Railway Monitoring Using Satellite SAR Interferometry

Ling Chang, Rolf P. B. J. Dollevoet, and Ramon F. Hanssen, *Senior Member, IEEE*

***Abstract*—Satellite synthetic aperture radar interferometry (InSAR) has the capability to monitor railway tracks and embankments with millimeter-level precision over wide areas. The potential of detecting differential deformation along the tracks makes it one of the most powerful and economical means for monitoring the safety and stability of the infrastructure on a weekly basis. Yet, the mere capability to detect such small deformations is not sufficient for an operational application of the technique. Handling huge data volumes, homogenizing independent datasets, and the connection with expert knowledge to identify risk areas are challenges to overcome. Here, we use a probabilistic method for InSAR time series postprocessing to efficiently scrutinize the data and detect railway instability. Moreover, to detect high-strain segments of the railway, we propose a short-arc-based method to focus on localized differential deformation between nearby InSAR measurement points. Our approach is demonstrated over the entire railway network of the Netherlands, more than 3000 km long, using hundreds of Radarsat-2 acquisitions between 2010 and 2015, leading to the first satellite-based nationwide railway monitoring system.**

***Index Terms*—Railway infrastructure, satellite, synthetic aperture radar (SAR), synthetic aperture radar interferometry (InSAR), testing theory.**

I. Introduction

IRREGULAR settlement of railways, e.g., due to traffic loads, ageing, or local ground movement, impacts its structural stability and the safety of passengers on board [1]. Conventional methods for structural health monitoring of railway use *in-situ* measurement devices, such as GPS [2], [3], leveling [4], or the deployment of special survey trains [5]. These methods are generally labor intensive, expensive, and can, therefore, only be applied on a limited scale, either in space or time. Moreover, these methods are usually only deployed at locations where structural deformation is suspected, requiring *a priori* knowledge that may not be available everywhere. Using satellite Synthetic Aperture Radar Interferometry (InSAR) techniques [6], [7], we are able to complement these conventional methods and monitor the kinematic behavior (strain or deformation) of railway infrastructure over wide areas, with millimeter precision, for the detection of track or embankment instability [5], [8], [9].

Manuscript received February 12, 2016; revised May 18, 2016; accepted June 22, 2016. Date of publication July 27, 2016; date of current version January 23, 2017. *(Corresponding author: Ling Chang.)*

L. Chang and R. P. B. J. Dollevoet are with the Department of Structural Engineering, Delft University of Technology, Delft 2628 CN, The Netherlands (e-mail: L.Chang@tudelft.nl; R.P.B.J.Dollevoet@tudelft.nl).

R. F. Hanssen is with the Department of Geoscience and Remote Sensing, Delft University of Technology, Delft 2628, CN, The Netherlands (e-mail: R.F.Hanssen@tudelft.nl).

Color versions of one or more of the figures in this paper are available online at http://ieeexplore.ieee.org.

Digital Object Identifier 10.1109/JSTARS.2016.2584783

Aiming for a nationwide systematic railway monitoring system, with continuous temporal updates, and an automatic detection and identification functionality for railway areas at risk, it is necessary to digest huge—continuously increasing—data volumes, and to connect data acquired from different satellite positions in the same geodetic datum. Moreover, to automatically detect risk areas, experts in the railway domain should identify threshold values for the parameters of interest.

In this study, we use Persistent Scatterer InSAR [10], [11] to generate kinematic time series of millions of measurement points. The motion of each InSAR measurement point is relative to the motion of a predefined reference point. We use a probabilistic method for InSAR time-series postprocessing [12] to estimate the most probable displacement parameters for each point in order to detect irregular railway settlement. First, we use an expandable library of canonical kinematic functions, which subtends all the deformation mechanisms that are deemed to be of concern. The kinematic functions are physically realistic, for example, to detect sequential settlement, sudden offsets, or temperature-related deformation. Then, we determine the best-fit model parameterization per InSAR measurement point using multiple hypothesis testing. Eventually, we

1) estimate millimeter-level settlements;
2) generate deformation maps along the railway;
3) evaluate the quality of the estimated deformations per measurement point;
4) classify the InSAR measurement points along the railway in terms of temporal behavior.

Since there are millions of measurement points and hundreds of epochs, we use an efficient implementation to test hundreds of models [12], [13] and report significance levels for the estimated parameters.

This paper is organized as follows. A brief description of the Dutch railways and the applied SAR data are presented in Section II. Section III is dedicated to the method of automatic railway settlement detection. This method is applied on the settlement detection of the entire railway network of the Netherlands. In Section IV, the results of the Dutch railway network are discussed. Conclusions are drawn in Section V.

II. Dutch Railways and Satellite Sampling

The Dutch railway network is heavily utilized with a total route length of 3223 km, indicated by the black lines in Fig. 1. The stability of the railway network is an operational requirement of high importance, considering continuously increasing traffic loads and ageing, especially in the Rhine–Meuse–Scheldt

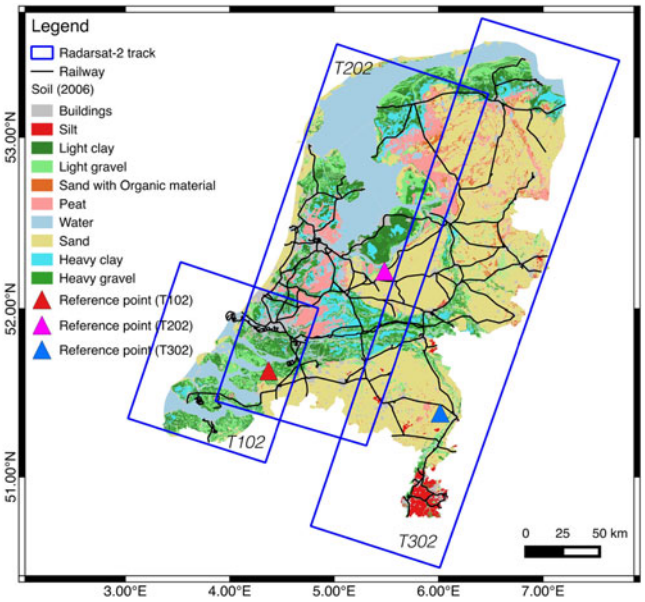

Fig. 1. Dutch railway system superimposed on a soil map (1:50 000, 2006), indicating different degrees of presumed stability. Three Radarsat-2 tracks, T102, T202, and T302, (in blue) cover the entire Dutch railways. In total, 213 different satellite acquisitions were used. The reference points of tracks T102, T202, and T302 are indicated by the red, purple, and blue triangle, respectively.

TABLE I
RADARSAT-2 SAR DATA USED

Track Nr.	Start/End Date	Acquisitions
T102	2010-06-13 – 2015-06-11	72
T202	2010-06-20 – 2015-08-05	69
T302	2010-06-03 – 2015-06-25	72

delta where most soils are hydromorphic [14]. About 90% of these soils have a ground water depth of less than 140 cm in winter [15]. Dominant soil types are clay, peat, gravel, and sand (see Fig. 1). Although the Dutch railways have been designed to withstand the hydromorphic soil conditions, in practice, they do deform and need to be regularly inspected and maintained.

We use a stack of Radarsat-2 C-band SAR images acquired between June 2010 and August 2015 (tracks: T102, T202, and T302), with a 24-day satellite repeat cycle, as shown in Fig. 1. These three tracks cover the railway network of the Netherlands. There are 72, 69, and 72 images for tracks T102, T202, and T302, respectively (see Table I). The HH polarization mode is used, since the HV time series has a limited number of acquisitions. All tracks are acquired from the descending orbit. The ground range and azimuth resolution of each SAR image are ∼22 and 7.6 m, respectively. We oversample all SAR images by a factor of 2 to avoid aliasing during interferogram formation and reduce the pixel size of every SAR image to ∼13 and ∼4 m in ground range and azimuth, respectively.

III. METHOD

The Delft implementation of Persistent Scatterer InSAR is applied on the available SAR data tracks [10], [11], [16], followed by the geocoding of all results to the ETRS89 reference system. Since different independent partly overlapping satellite tracks need to be combined, we first elaborate on the applied method for multitrack datum connection that is required to bring all time series in the same geodetic datum. This is followed by our "short-arc" strategy, aimed to detect high strain rate locations. As every short arc could have a different temporal behavior, we evaluate each arc against a library of canonical functions to find the model that fits the data best, using a multiple hypothesis testing method.

A. Multitrack Processing

InSAR time series are all relative to a specific reference point or area. Since we use three tracks of Radarsat-2 SAR images, each track has a different reference point, indicated by the red/purple/blue triangles in Fig. 1. To connect these time series to a common datum, a datum transformation is required (see Fig. 2). We apply a three-step procedure. First, we estimate and mitigate the noise and motion of the reference point using the Shenzhen algorithm proposed by [12]. Second, we select hundreds of point pairs from the overlapping region of two adjacent tracks, each pair-member from a different track, with a spatial distance of less than 1 m, and use them as tie points. As the time of the reference SAR acquisition and the location of the reference point are different for each track, the displacement time series have a different starting time and a different velocity, respectively, for each pair of tie points. Thus, assuming steady-state motion, an unknown velocity difference $\Delta\dot{d}_{r,r'}$ for the point pair p and q in Fig. 2(b) has to be accounted for. For track T_1, the distance D to the satellite at time t can be expressed for point p and r as

$$\begin{aligned} D_p(t) &= (t-t_0)\dot{D}_p + D_p(t_0) \\ D_r(t) &= (t-t_0)\dot{D}_r + D_r(t_0) \end{aligned} \tag{1}$$

respectively, where the time of the reference (master) acquisition is t_0, the (unknown) displacement line-of-sight velocities of point p and r are $\dot{D}_p$, $\dot{D}_r$, and the (unknown) absolute distances at time t_0 for point p and r are denoted as $D_p(t_0)$ and $D_r(t_0)$, respectively. The line-of-sight distance difference $d_{p,r}$ of point p w.r.t. the reference point r at time t can now be written as

$$\begin{aligned} d_{p,r}(t) &= D_p(t) - D_r(t) \\ &= (t-t_0)(\dot{D}_p - \dot{D}_r) + (D_p(t_0) - D_r(t_0)) \\ &= (t-t_0)\dot{d}_{p,r} + d_{p,r}(t_0) \end{aligned} \tag{2}$$

where $\dot{d}_{p,r}$ and $d_{p,r}(t_0)$ represent the relative velocity and distance difference at t_0, for point p w.r.t. point r. Note that in this equation, no assumptions on the distance or stability of the reference point r need to be made. If we cast this in a system of observation equations, we find

$$\underline{d}_{p,r,t_0}(t) = \underline{d}_{p,r}(t) - \underline{d}_{p,r}(t_0) = (t-t_0)\dot{d}_{p,r} \tag{3}$$

where the double (spatiotemporal) differences $\underline{d}_{p,r,t_0}(t)$ are the $m \times 1$ vector of observations (for $m+1$ acquisitions) and $\dot{d}_{p,r}$ (the difference between the velocities of reference point r and point p) is the unknown line-of-sight velocity difference. The underlines indicate the stochastic character of the observables. Note that (3) implies that a model fit through the observed

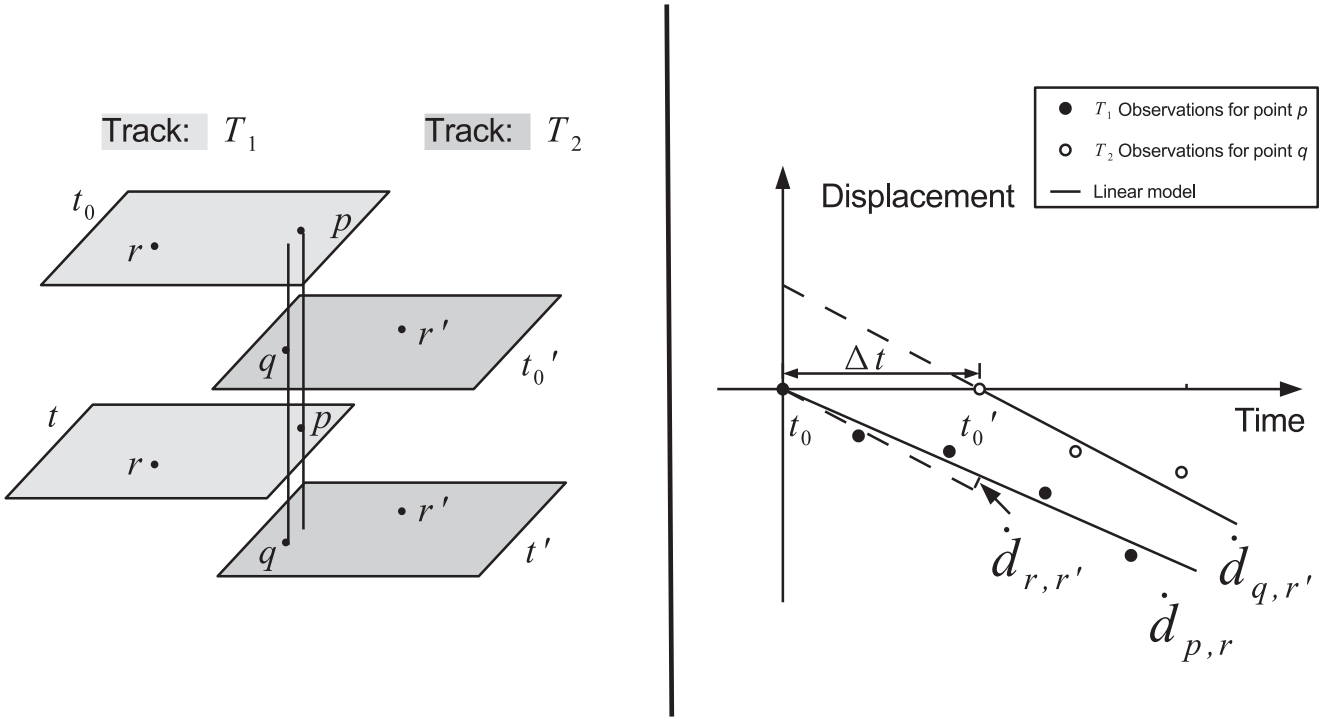

(a) (b)

Fig. 2. Schematic graph for datum connection. (a) In the overlapping area of track T_1 and T_2, a tie-point pair, point p and q, is assumed to exhibit the same displacement behavior. However, the measured displacement time series of point p and q are different, since they are relative to reference point r for track T_1 and r' for track T_2. (b) $\dot{d}_{p,r}$ and $\dot{d}_{q,r'}$ are the linear velocity estimators for track T_1 and T_2, respectively, for a tie-point pair $(p,\ q)$. $\dot{d}_{r,r'}$ is the velocity difference and Δt is the known (time) offset between the master acquisitions, t_0 and t_0', of track T_1 and T_2, respectively. The acquisition times are t_0, t_0', t and t'.

double-difference time series is by definition forced through the $(t_0, 0)$ coordinate.

Likewise, for track T_2, the displacement of point q w.r.t. reference point r' at time t can be written as

$$\underline{d}_{q,r',t_0'}(t) = \underline{d}_{q,r'}(t) - \underline{d}_{q,r'}(t_0') = (t - t_0')\dot{d}_{q,r'} \tag{4}$$

where $t_0' = t_0 + \Delta t$ is the time of the reference (master) acquisition of track T_2 [see Fig. 2(b)]. The displacement of any point q in track T_2 can be linked to the reference point r of track T_1, if the motion of reference point r' in T_2 would be known relative to reference point r in track T_1. For this, we rewrite (4) as

$$\underline{d}_{q,r',t_0'}(t) = (t - t_0')(\dot{d}_{q,r} + \dot{d}_{r,r'}) \tag{5}$$

or, expressed relative to t_0, as

$$\underline{d}_{q,r',t_0}(t) = (t - t_0 - \Delta t)\dot{d}_{q,r} + (t - t_0 - \Delta t)\dot{d}_{r,r'}. \tag{6}$$

Since $\dot{d}_{q,r}$ and $\dot{d}_{r,r'}$ are lumped together in (5), they cannot be estimated independently. However, assuming that the selection of (many) point pairs p and q in T_1 and T_2, respectively [see Fig. 2(a)] follows the same kinematic behavior, we force $E\{\dot{d}_{p,r} - \dot{d}_{q,r}\} = 0$; hence, combining (3) and (6) yields

$$\dot{\underline{d}}_{r,r'} = \frac{\underline{d}_{q,r',t_0}(t)}{t - t_0 - \Delta t} - \frac{\underline{d}_{p,r,t_0}(t)}{t - t_0}. \tag{7}$$

Thus, introducing the known horizontal time offset Δt, the unknown velocity difference between the two reference points $\dot{\underline{d}}_{r,r'}$ can be estimated. To avoid errors due to outliers, we use a large number of tie-point pairs $(p,\ q)$ and perform a least-squares adjustment to estimate the velocity difference between tracks.

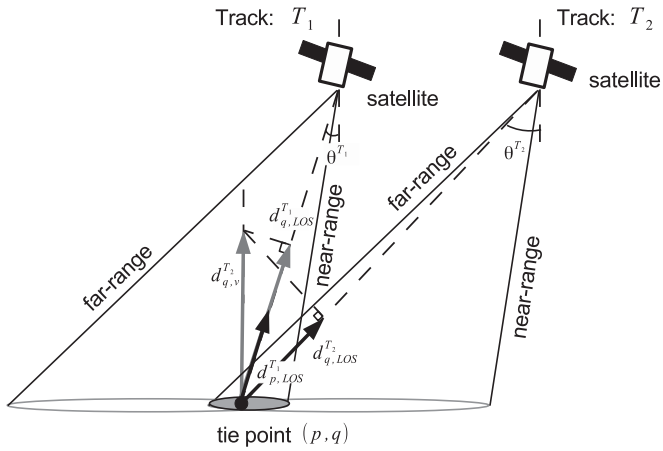

Fig. 3. Line-of-sight motion and back-projection of a tie point. In the overlapping region of two adjacent tracks, e.g., T_1 and T_2 (shown in gray), the incidence angles (θ^{T_1} for track T_1 and θ^{T_2} for track T_2) for a tie point $(p,\ q)$ (black dot) are different. The observed line-of-sight motion of the tie point from track T_1 and T_2 is denoted as $d^{T_1}_{p,\mathrm{LOS}}$ and $d^{T_2}_{q,\mathrm{LOS}}$, respectively, which is linked via the vertical motion $d^{T_2}_{q,v}$ assuming the dominant part is vertical, when considering the adjustment of a large number of tie points. The back-projected line-of-sight motion from track T_2 to T_1 is denoted as $d^{T_1}_{q,\mathrm{LOS}}$.

It is worth noting that to connect two time series from adjacent tracks, e.g., T_1 and T_2, the differences in incidence angles for tie-point pairs need to be taken into account (see Fig. 3). Given the large amount of tie-point pairs, we assume that the dominant part of the line-of-sight movement is vertical. In this respect, per

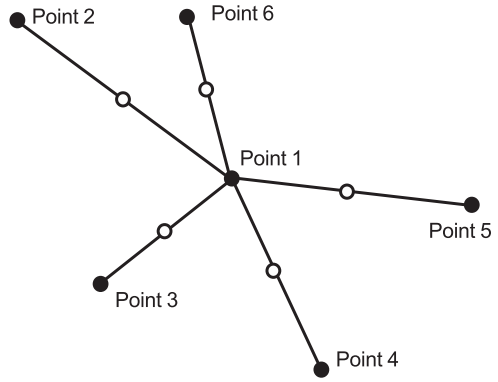

Fig. 4. Schematic graph for short-arc evaluation. Six InSAR measurement points 1–6 are shown as solid dots. The points 2–6 are spatially close to point 1. Five short arcs, the black solid lines, are built by individually linking points 2–6 to point 1. The temporal behavior of each short arc will be attributed to the virtual center point in the black circle.

tie point $(p,\ q)$ as shown in Fig. 3, we back-project the line-of-sight motion $d^{T_2}_{q,\mathrm{LOS}}$ in track T_2 to the line-of-sight motion $d^{T_1}_{p,\mathrm{LOS}}$ in track T_1, that is denoted as $d^{T_1}_{q,\mathrm{LOS}}$, via the vertical motion $d^{T_2}_{q,v}$. The back-projection conversion is defined as

$$d^{T_1}_{q,\mathrm{LOS}} = \frac{\cos\theta^{T_1}}{\cos\theta^{T_2}} \cdot d^{T_2}_{q,\mathrm{LOS}} \tag{8}$$

where the incidence angles in track T_1 and T_2 are θ^{T_1} and θ^{T_2}, respectively.

B. Short Arc

Localized deformation yields high strain rates, which are more important for railway stability than wide-scale deformation. Therefore, we focus on the detection of localized railway settlement by using hypothesis testing on differential deformation between two nearby InSAR measurement points (i.e., short arcs). For a certain InSAR measurement point, such as point 1 in Fig. 4, we can build several short arcs (five short arcs in this case), shown as the black lines. To indicate the kinematic temporal behavior of each arc, in the following, we will use the virtual center point of each short arc. We then compute the kinematic double-difference time series with respect to center point 1.

C. Modeling

The temporal behavior of every short arc is different and can be parameterized by various physically realistic parameters. In the "steady-state" mode, each short arc is parameterized as a linear function of time. It means that the two linking points for the short arc behave similarly, and their difference behaves linear in time. We treat the "steady-state" model as the default model (the null hypothesis H_0). This linear function can be written as $M_1(\dot{d}) = (t - t_0)\dot{d}$, where $t - t_0$ is the temporal baseline w.r.t. the reference (master) image acquisition at t_0, and $\dot{d}$ represents the (relatively) constant linear velocity. When one of the two linking points of a certain short arc does not follow this default model, an alternative model is required. Hence, against the null hypothesis, we build a library with several canonical functions for testing the potentially best-fit models, such as the following.

1) *Temperature-related function:* $M_2(\eta) = \Delta T \cdot \eta$, where the thermal expansion $\eta = \mu_{\Delta T} \cdot L_{\mathrm{LOS}}$ ($\mu_{\Delta T}$ is the linear expansion coefficient and L_{LOS} is the dimension of the object in the LOS direction [17], [18]), and ΔT [K] represents the temperature difference between the slave and master acquisition.
2) *Step function:* $M_3(\Delta_i) = \Delta_i \mathcal{H}(t - \tau_i),\ i \in [1,\ m-1]$, where $\mathcal{H}(t - \tau_i)$ is the Heaviside Step function, centered at τ_i [19]. The offset Δ_i occurs between t_{i-1} and t_i.
3) *Breakpoint function:* $M_4(\dot{d}_1, \dot{d}_2) = t^a \cdot \dot{d}_1 + t^b \cdot \dot{d}_2,\ t^a \in [1, j],\ t^b \in [j+1, m]$, where t^a and t^b are temporal baselines between the slaves and master acquisition, and $\dot{d}_1$ and $\dot{d}_2$ are the linear velocities for two distinct time spans. Note that this single-breakpoint model can be extended to double-, or triple-, breakpoint models, given *a priori* information by sequentially evaluating all possible positions.

With those canonical functions, many alternative hypotheses $(H_j, \forall j)$ can be built, in order to find the best model among them. The mathematical expressions of the null hypothesis H_0 and all possible alternative hypotheses $H_j, \forall j$, are given by

$$\begin{aligned}
H_0: \quad & \underset{m\times 1}{E\{\underline{d}\}} = \underset{m\times n}{A}\,\underset{n\times 1}{x}, \\
& \underset{m\times m}{D\{\underline{d}\}} = \underset{m\times m}{Q_{\mathrm{dd}}} = \sigma^2 R_{\mathrm{dd}} \\
H_j: \quad & \underset{m\times 1}{E\{\underline{d}\}} = \underset{m\times n}{A}\,\underset{n\times 1}{x} + \underset{m\times q}{C_j}\,\underset{q\times 1}{\nabla_j}, \nabla_j \neq 0, \\
& \underset{m\times m}{D\{\underline{d}\}} = \underset{m\times m}{Q_{\mathrm{dd}}} = \sigma^2 R_{\mathrm{dd}}
\end{aligned} \tag{9}$$

where A is the design matrix, $E\{\cdot\}$ is the expectation operator, m is the number of observations $\underline{d}$, and n is the number of unknowns x. In our case, A is the matrix of temporal baselines [year] between the slave images and the master image, x is the linear velocity, $\dot{d}$, [mm/year]. Any alternative hypothesis is defined by a specification matrix C_j and an additional new vector of unknown parameters ∇_j of the dimension (or degree of freedom) q, with $q \in [1, m-n]$. The dispersion D of the observations is given using the variance of unit weight σ^2 and the cofactor matrix R_{dd} of the covariance matrix Q_{dd}. The additional component $C_j \nabla_j$ may represent (a combination of) $M_2(\eta),\ M_3(\Delta_i),\ M_4(\dot{d}_1, \dot{d}_2)$. The functional models of all hypotheses are then written as, e.g.,

$$\begin{aligned}
H_0:\ & M_1(\dot{d}) && \\
H_1:\ & M_1(\dot{d}) + M_2(\eta), && q = 1 \\
H_2:\ & M_1(\dot{d}) + M_2(\eta) + M_3(\Delta_i), && q = 2 \\
H_3:\ & M_1(\dot{d}) + M_3(\Delta_i), && q = 1 \\
H_4:\ & M_4(\dot{d}_1, \dot{d}_2), && q = 2.
\end{aligned} \tag{10}$$

Assuming that there may be only one step and only one breakpoint in the time series with m observations, $2(m-2)$ alternative models are required to be tested as both the step and the breakpoint may occur at any time between the start and end

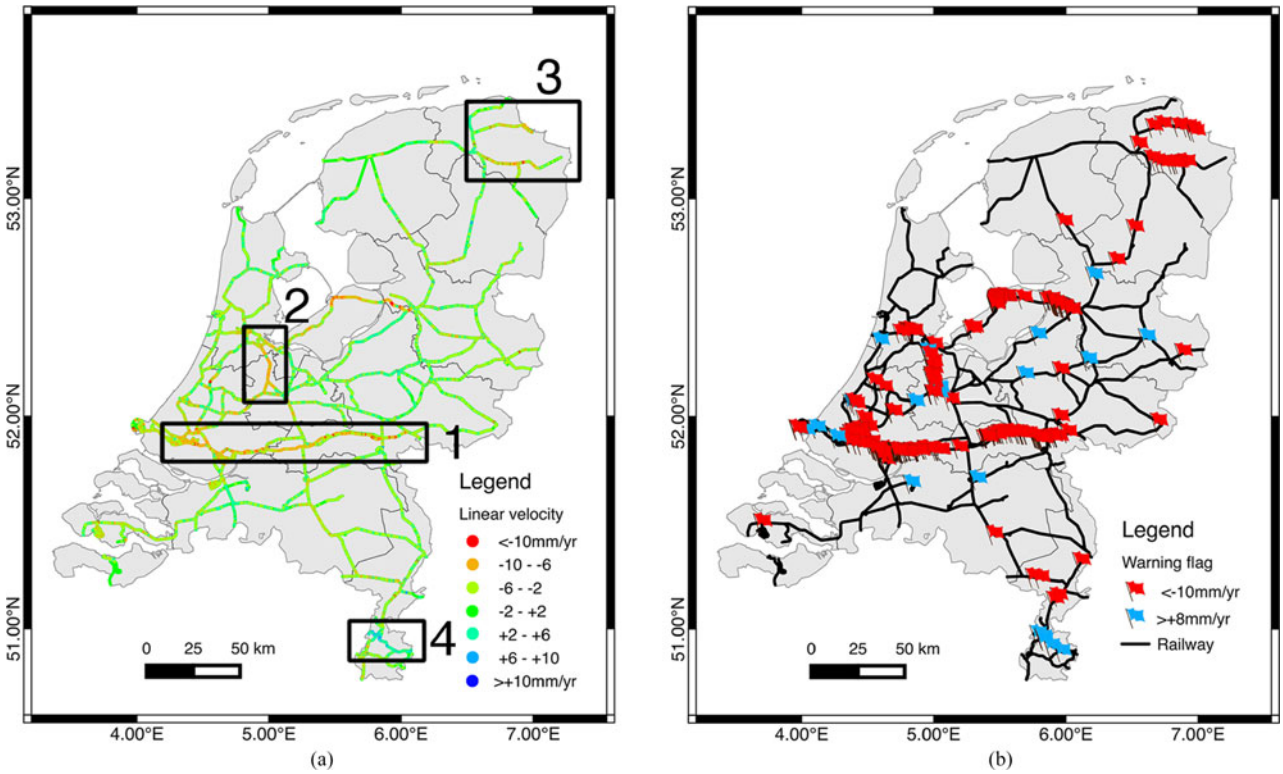

Fig. 5. (a) Line-of-sight deformation velocity map of the Netherlands. (b) Risk map, in which the colored flags indicate the severity of the deformation, as indicated by domain experts. Four areas of interest are indicated by the black rectangles in (a).

acquisition. Therefore, the amount of alternative models is far more than 4 as in (10), and it can easily reach to the order of hundreds.

D. Multiple Hypothesis Testing

Since we have more than one alternative hypothesis, and the alternative hypotheses have different dimensions, we use the test ratio, expressed as [20], [21]

$$\underline{\mathbf{T}}^j_{\mathrm{q_j}} = \underline{T}^j_{\mathrm{q_j}} / \chi^2_{\alpha_j}(q_j) \tag{11}$$

where $\chi^2_{\alpha_j}(q_j)$ is the critical value with a predefined level of significance α_j, and $\underline{T}^j_{\mathrm{q_j}}$ is the test statistic, defined as [21]

$$\underline{T}^j_q = \underline{\hat{e}}_0^T Q_{\mathrm{dd}}^{-1} C_j (C_j^T Q_{\mathrm{dd}}^{-1} Q_{\hat{e}_0 \hat{e}_0} Q_{\mathrm{dd}}^{-1} C_j)^{-1} C_j^T Q_{\mathrm{dd}}^{-1} \underline{\hat{e}}_0 \tag{12}$$

where the residual vector $\underline{\hat{e}}_0$ is the difference between the observations and the estimations in H_0, that is, $\underline{\hat{e}}_0 = \underline{d} - \underline{\hat{d}}_0$, ($\underline{\hat{d}}_0 = A(A^T Q_{\mathrm{dd}}^{-1} A)^{-1} A^T Q_{\mathrm{yy}}^{-1} \underline{d}$). The (co)variance matrix of the residual vector is expressed as $Q_{\hat{e}_0 \hat{e}_0} = Q_{\mathrm{dd}} - A(A^T Q_{\mathrm{dd}}^{-1} A)^{-1} A^T$.

If the ratio $\underline{\mathbf{T}}^j_{\mathrm{q_j}} > 1$, it means that $\underline{T}^j_{\mathrm{q_j}}$ exceeds the critical value; thereby, we reject the null hypothesis H_0 and find the best alternative model with the largest test ratio value among the alternative hypotheses. On the contrary, if $\underline{\mathbf{T}}^j_{\mathrm{q_j}} \leq 1$, we retain the null hypothesis H_0 as the best-fit model.

As the test ratio, as in (11), includes the (co)variance matrix Q_{dd} [see (9)], one needs to know the stochastic model of the observations. In practice, however, incomplete knowledge of the stochastic model $D\{\underline{d}\} = Q_{\mathrm{dd}}$ of the observation occurs in most cases. Therefore, if no other information is available, we start to build the covariance matrix Q_{dd} with a simple model consisting of a variance of unit weight σ^2 and cofactor matrix $R_{\mathrm{dd}} = \mathrm{I}$.

IV. Results and Discussion

Using 213 Radarsat-2 SAR images and the 90-m resolution DEM (SRTM, [22]) of the Netherlands, we performed a data-processing procedure, as described in Section III. The line-of-sight deformation linear velocity map of the Netherlands for the railways in the same reference coordinates is shown in Fig. 5(a). We defined a 50-m-wide buffer along the railways and extracted the PS points within this buffer. There are 95 881, 303 405, and 250 704 PS points along the railway tracks, acquired from T102, T202, and T302, respectively. Assuming that the vertical deformation (settlement) is dominant and the horizontal movement is marginal, the line-of-sight deformation (denoted as $\underline{d}_{\mathrm{LOS}}$) can be projected to the vertical direction by $\underline{d}_{\mathrm{LOS}}/\cos\theta$, where θ represents the incidence angle for these three Radarsat-2 scenes, i.e., $[30.6^\circ\ 37.1^\circ]$. Fig. 5(a) shows that 97% of the points are relatively stable ($\leq$6 mm/yr deformation velocity), shown in green, while 3% exhibits a significant deformation trend, identifying potential high-strain segments of the railways. To evaluate the severity of the deformation, we build a "flagging system," shown in Fig. 5(b). The areas with <-10 mm/yr deforming rate and $>+8$ mm/yr uplifting rate are highlighted by the red and blue flags, respectively, based on expert consultation. The risk map shows the following.

1) The Betuwe (freight) railway (denoted as 1) is deforming extremely fast. The railway segment between Amsterdam

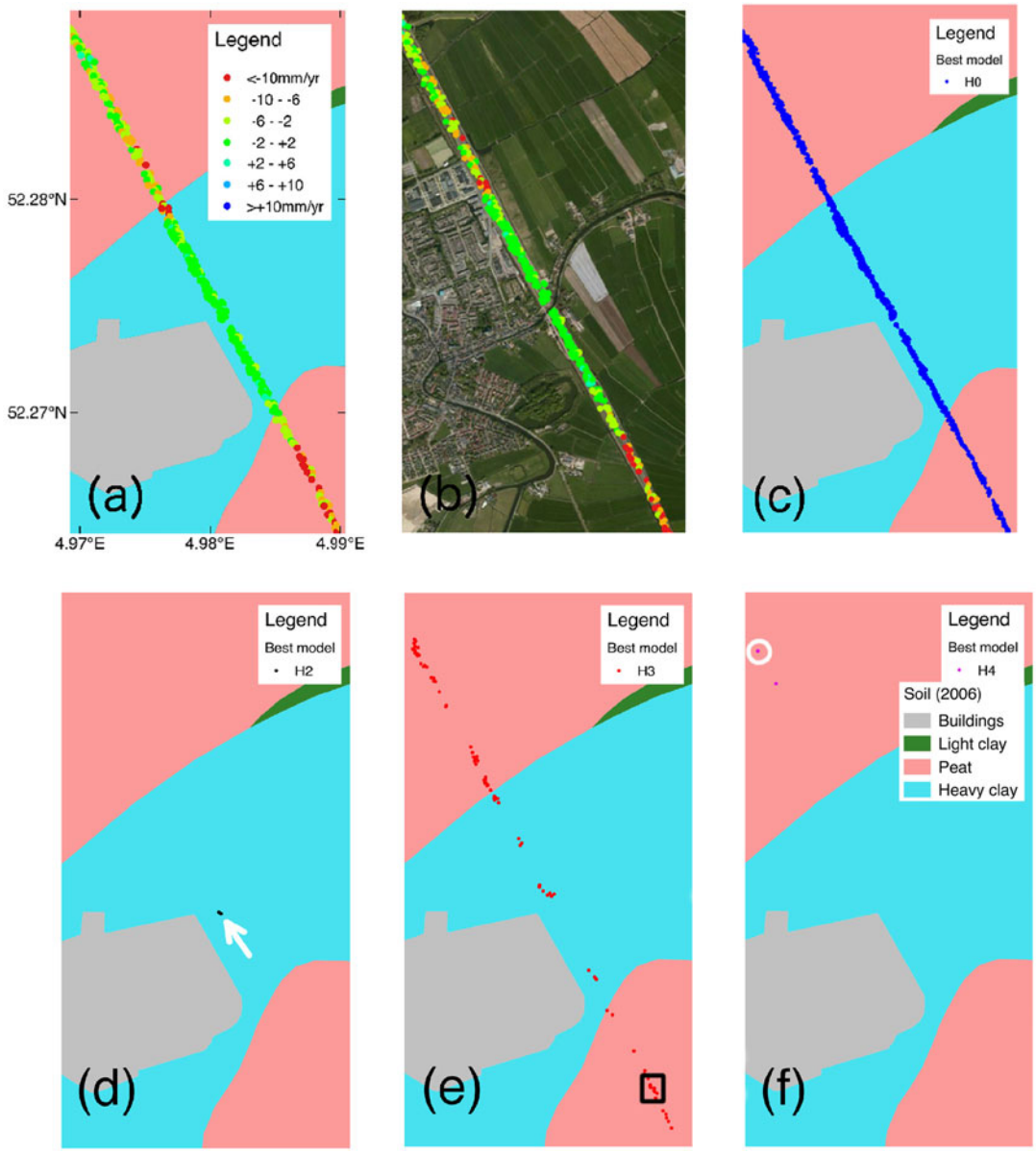

Fig. 6. Line-of-sight deformation velocity of the InSAR measurements along the railway, over a small crop area, on top of the soil map (a) and optical imagery (b). (c)–(f) show the best models for the short arcs, i.e., steady-state (c), steady-state, temperature and step (d), steady-state and step (e), and breakpoint (f). The models are listed in (10). The time series of the white-circled short arc in (f) are shown in Fig 9. Note that the background soilmap has a poor (outdated) accuracy for the built-up area.

and Utrecht (the "A2-corridor"), where the speed of trains is 160 km/h (denoted as 2), is deforming fast as well.

2) The railways in the Groningen province (denoted as 3) are subsiding. This is due to the production of natural gas in this region; cf., [23].
3) The railways in the southern part of Limburg (denoted as 4) are moving upwards, due to the subsurface water rebound after coal mining activities in the last century.

The rising waters cause the land, including the railways, to uplift; cf., [24]. Apart from these regions, the flags of Fig. 5 show several other localized anomalies in railway stability. In short, all areas with colored flags require further *in-situ* analysis.

The map of Fig. 5 gives a good nationwide overview of problematic areas, but is too coarse to identify very localized instabilities, where they occur and when they occur. For this objective, short arcs are analyzed using multiple hypothesis testing. We initialized the value of the variance of unit weight σ^2 for the short arcs to be 8^2 mm^2. All potential models listed in (10) are tested.

Fig. 6 shows the small-arc results for a test area. The line-of-sight deformation velocities of the InSAR measurements along the railway are shown in Fig. 6(a). It suggests that 1) subsidence is more considerable over the peat soils (pink) than in heavy clay soils (light blue); and 2) at the transition zones between two different soil types (i.e., peat and heavy clay), a strong differential subsidence is detected. The ground features in this area are shown on the optical imagery (June 2015) in Fig. 6(b). We applied multiple hypothesis testing for all potential models of

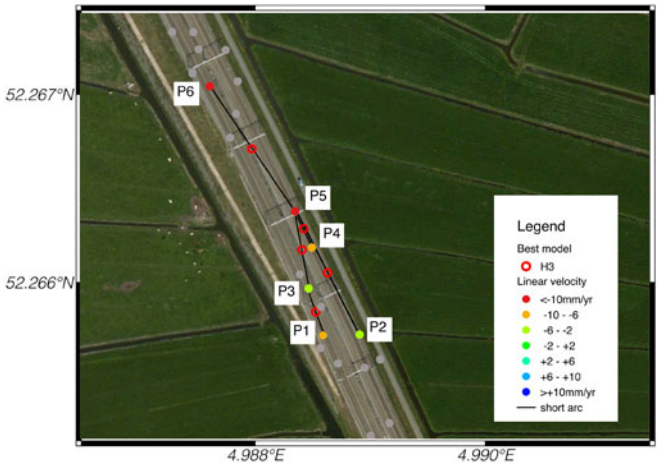

Fig. 7. Five short arcs (black lines): P1-P3, P2-P5, P3-P5, P4-P5, and P5-P6 for six PS points P1–P6, for an area indicated by the black square in Fig. 6(e). All these short arcs follow the H_3 (step) hypothesis, indicated by the red circle. The solid dots show the locations of the InSAR measurement points, and the color represents the line-of-sight linear velocity. The other surrounding PS points are shown in gray.

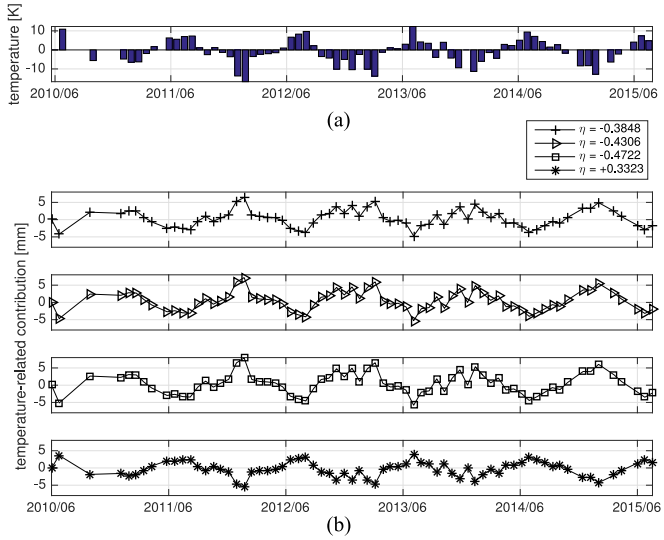

Fig. 8. (a) Temperature difference (ΔT [K]) w.r.t. the first acquisition (T202). (b) Temperature-related contributions for four short arcs with different temperature-related parameter estimators η.

(10), and the best models for the short arcs over this crop area are shown in Fig. 6(c)–(f). Here, we built five short arcs for every measurement point (cf., Fig. 4) and the maximum spatial distance between the linking points (for building a short arc) is 50 m. Fig. 6(c) shows that the temporal behavior of 95% of the short arcs follow the "steady-state" model, which implies that most of the short arcs are either stable or linearly deforming. There are a few short arcs following alternative hypotheses [see Fig. 6(d)–(f)]. For instance, the red points in Fig. 6(e) represent short arcs follow H_3, with an irregular offset (or jump) in time. In Fig. 6(c)–(f), we show the results for the virtual center points of the short arcs, instead of the InSAR measurement points, due to the limited information that can be conveyed in such a large-scale map (in this case). As an example, we give more details for the black square shown in Fig. 6(e). Fig. 7 shows five short arcs as black lines, linking P1-P3, P2-P5, P3-P5, P4-P5, and P5-P6. These five short arcs follow the H_3 hypothesis (indicated by the red circle). The solid dots show the locations of the InSAR measurement points, while the color represents the line-of-sight deformation velocity. The kinematic time series of the six points P1–P6 and the corresponding five short arcs are shown in Fig. 10. In the left column, the time series of the six points w.r.t. a common reference point (denoted by the purple triangle in Fig. 1) are presented. The default steady-state model for each point is shown by the solid line. In the right column of Fig. 10, the time series (in the black cycles) of the corresponding five short arcs, i.e., P1-P3, P2-P5, P3-P5, P4-P5, and P5-P6, are shown, including the optimal model result of the multiple hypothesis testing approach, in red. This demonstrates the added information content of the short-arc time series over the conventional time series w.r.t. a common reference point. The estimated linear velocities under H_0 are listed in Table II, as well as the hypothesis testing results for the short arcs. It is clear that sudden anomalous temporal changes may occur over short arcs, even when the linear velocities of the two points are

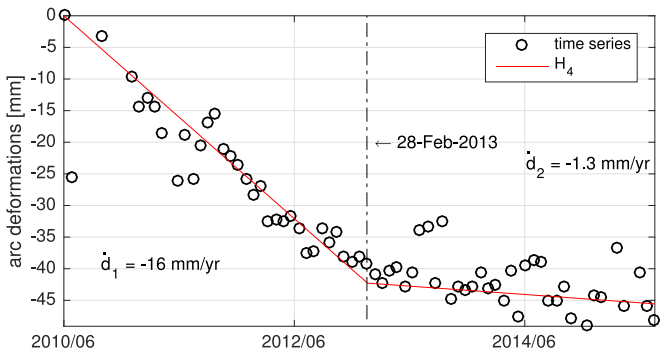

Fig. 9. Short arc with the best model: H_4. The break point happens at February 28, 2013. The location of this arc is circled in white in Fig. 6(f).

only slightly different, as, e.g., points P5 and P6. The short-arc analysis for two points will cancel out the temporal similarity between these two points, while distinctly showing the temporal differences between them. According to the results in Table II, we conclude that 1) the (square-roots of the) posterior variances $\hat{\underline{\sigma}}^2$ of the five short arcs are smaller than the conservative *a-priori* variances ($\sigma = 8$ mm) which improves the reported quality of the estimates and the time series; and 2) point P5 exhibits an irregular shift between 30 January and 19 March 2014, compared with its surroundings. This temporal jump (or offset) is around 20 mm, compared with points P2, P3, P4, and P6.

Apart from the short arcs keeping either H_0 (steady-state) or H_3 (steady-state + step) hypothesis, 1% of the short arcs hold H_2 (including temperature) or H_4 (breakpoint). We illustrate the temperature-related contributions for four arbitrarily selected short arcs with different temperature-related parameter estimators η in Fig. 8(b). The amplitude of the temperature-related contributions can be calculated by $\Delta T \cdot \eta$. The temperature difference (ΔT [K]) w.r.t. the first acquisition (June 20,

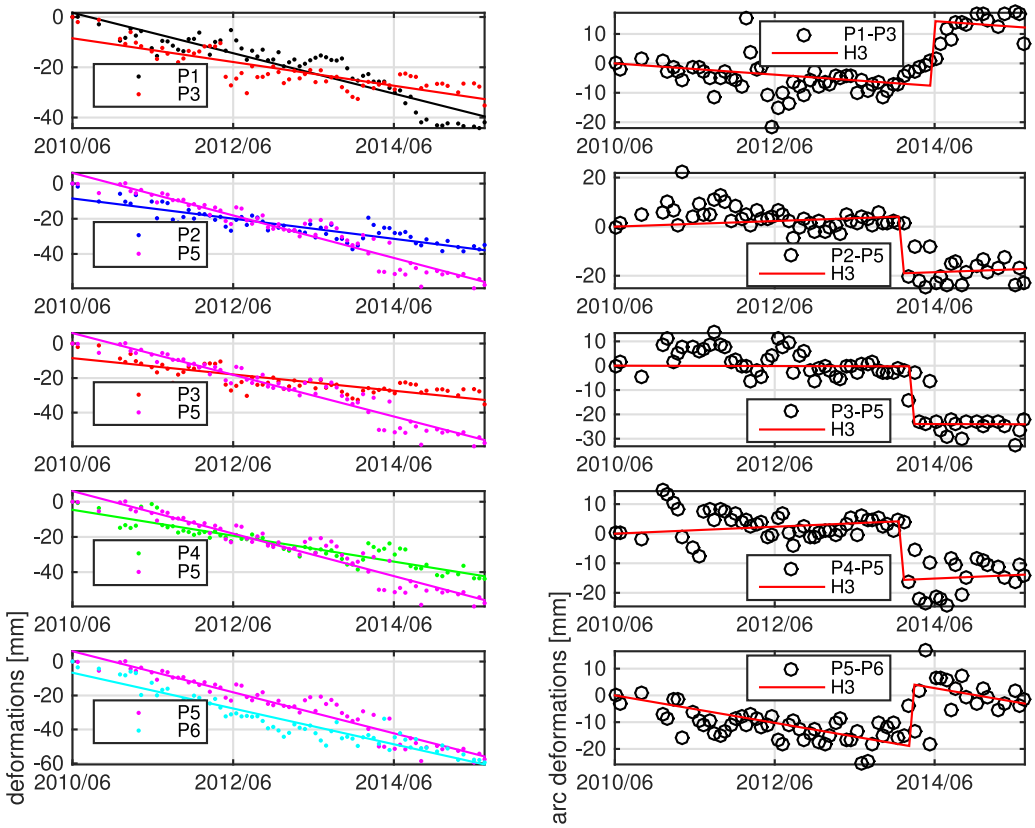

Fig. 10. Time series (in the color dots) of the six points w.r.t. a common reference point, with the null hypothesis H_0: linear model in the solid lines, in the left column. The time series (in the black circles) of the five short arcs: P1-P3, P2-P5, P3-P5, P4-P5, and P5-P6, accompanying with the best model in red, in the right column. The models are listed in (10).

TABLE II
PARAMETER ESTIMATION TABLE, LISTING THE ESTIMATED LINEAR DEFORMATION VELOCITIES UNDER THE NULL HYPOTHESIS H_0 PER POINT, AND THE HYPOTHESIS TESTING RESULTS FOR THE SHORT ARCS

Point	P1	P2	P3	P4	P5	P6
$\hat{d}(H_0)$ [mm/year]	−8.0	−5.7	−4.7	−7.3	−12.1	−10.5
Short arc	P1-P3	P2-P5	P3-P5	P4-P5	P5-P6	–
$\hat{d}(H_3)$ [mm/year]	−1.9	1.1	−0.1	1.2	−5.1	–
$\hat{\Delta}(H_3)$ [mm]	22.0	−23.2	−23.7	−19.9	23.2	–
Acquisition date	23-Jun-2014	30-Jan-2014	19-Mar-2014	30-Jan-2014	19-Mar-2014	–
var.factor	0.43	0.44	0.49	0.40	0.50	–
$\underline{\hat{\sigma}}$ [mm]	5.3	5.3	5.6	5.1	5.7	–

2010, T202) is shown in Fig. 8(a). When the estimator of η is positive, it implies that the motions of ground targets are subject to temperature variations in the form of expansion when temperature rises and contraction when temperature falls. Considering the thermal expansion signatures of different materials, targets made of concrete or steel, such as railway lines, are mostly likely to have positive η values, while targets influenced by compaction due to seasonal changes in the groundwater table have negative η values. Short arcs best modeled by H_4 (breakpoint model) have two distinct linear trends before and after the breakpoint, e.g., the short arc shown in Fig. 9. The location of this arc is encircled in white in Fig. 6(f).

V. CONCLUSION

We demonstrated the feasibility of using satellite-based InSAR for monitoring railway infrastructure over a nationwide scale. We integrated 213 acquisitions over three independent satellite tracks to estimate the kinematic time series of millions of InSAR measurements over all railways in the Netherlands. The estimated displacements show several track segments with significant signal, dominantly subsidence-related. Especially, for hydromorphic soils (e.g., peat soils) in combination with recently constructed railway tracks, considerable instabilities are detected and flagged as such in a railway risk map. Localized high-strain segments are identified using a novel short-arc processing approach in combination with a hypothesis testing methodology. This approach allows us to optimally classify the deformation behavior to identify, e.g., sudden jumps, temperature-dependent variations, or trend-changes, which assists in finding the driving mechanisms behind the deformations. This way, the short-arc approach facilitates a user-initiated risk definition to create risk maps which are optimally tuned to their needs. A systematic application of satellite-assisted railway monitoring will increase the efficiency of asset management and improve overall railway safety.

ACKNOWLEDGMENT

The authors would like to thank the Netherlands Space Office for making Radarsat-2 data routinely available, and SkyGeo for assistance in data handling and WebGIS support, and the helpful comments of two anonymous reviewers and Dr. F. van Leijen. ProRail is acknowledged for valuable input and feedback.

REFERENCES

[1] C. Esveld, *Modern Railway Track*. Zaltbommel, Netherlands: MRT-Productions, 2001.
[2] J. Lovse, W. Teskey, G. Lachapelle, and M. Cannon, "Dynamic deformation monitoring of tall structure using GPS technology," *J. Surveying Eng.*, vol. 121, no. 1, pp. 35–40, 1995.
[3] A. Lepadatu and C. Tiberius, "GPS for structural health monitoring—Case study on the Basarab overpass cable-stayed bridge," *J. Appl. Geodesy*, vol. 8, no. 1, pp. 65–86, 2014.
[4] F. Chen, H. Lin, Z. Li, Q. Chen, and J. Zhou, "Interaction between permafrost and infrastructure along the Qinghai–Tibet Railway detected via jointly analysis of C-and L-band small baseline SAR interferometry," *Remote Sens. Environ.*, vol. 123, pp. 532–540, 2012.
[5] L. Chang, R. Dollevoet, and R. F. Hanssen, "Railway infrastructure monitoring using satellite radar data," *Int. J. Railway Technol.*, vol. 3, pp. 79–91, 2014.
[6] A. Ferretti, C. Prati, and F. Rocca, "Nonlinear subsidence rate estimation using permanent scatterers in differential SAR interferometry," *IEEE Trans. Geosci. Remote Sens.*, vol. 38, no. 5, pp. 2202–2212, Sep. 2000.
[7] R. F. Hanssen, *Radar Interferometry: Data Interpretation and Error Analysis*. Dordrecht, Netherlands: Kluwer, 2001.
[8] G. Liu *et al.*, "Exploration of subsidence estimation by persistent scatterer InSAR on time series of high resolution TerraSAR-X images," *IEEE J. Sel. Topics Appl. Earth Observ. Remote Sens.*, vol. 4, no. 1, pp. 159–170, Mar. 2011.
[9] Q. Luo, D. Perissin, H. Lin, Y. Zhang, and W. Wang, "Subsidence monitoring of Tianjin suburbs by TerraSAR-X persistent scatterers interferometry," *IEEE J. Sel. Topics Appl. Earth Observ. Remote Sens.*, vol. 7, no. 5, pp. 1642–1650, May 2014.
[10] A. Ferretti, C. Prati, and F. Rocca, "Permanent scatterers in SAR interferometry," *IEEE Trans. Geoscience Remote Sensing*, vol. 39, no. 1, pp. 8–20, Jan. 2001.
[11] B. Kampes, *Displacement Parameter Estimation Using Permanent Scatterer Interferometry* (ser. Forschungsbericht). Köln, Germany: DLR, Bibliotheks- und Informationswesen, 2005.
[12] L. Chang and R. F. Hanssen, "A probabilistic approach for InSAR time-series postprocessing," *IEEE Trans. Geosci. Remote Sens.*, vol. 54, no. 1, pp. 421–430, Jan. 2016.
[13] W. Baarda, *A Testing Procedure for Use in Geodetic Networks* (ser. Publications on Geodesy), vol. 5, 2nd ed. Delft: Netherlands: Geodetic Commission, 1968.
[14] H. De Bakker, *Major Soils and Soil Regions in the Netherlands*. New York, NY, USA: Springer, 2013.
[15] A. E. Hartemink and M. P. Sonneveld, "Soil maps of the netherlands," *Geoderma*, vol. 204, pp. 1–9, 2013.
[16] F. J. van Leijen, *Persistent Scatterer Interferometry Based on Geodetic Estimation Theory*. Delft: Netherlands: Geodetic Commission, 2014.
[17] O. Monserrat, M. Crosetto, M. Cuevas, and B. Crippa, "The thermal expansion component of persistent scatterer interferometry observations," *IEEE Geosci. Remote Sens. Lett.*, vol. 8, no. 5, pp. 864–868, Sep. 2011.
[18] M. Cuevas, O. Monserrat, M. Crosetto, and B. Crippa, "A new product from persistent scatterer interferometry: The thermal dilation maps," in *Proc. Joint Urban Remote Sens. Event*, 2011, pp. 285–288.
[19] E. W. Weisstein, "Heaviside step function," From *MathWorld–A Wolfram Web Resource*. 2008. [Online]. Available: http://mathworld.wolfram.com/HeavisideStepFunction.html
[20] H. M. de Heus, P. Joosten, M. H. F. Martens, and H. M. E. Verhoef, "Geodetische deformatie analyse: 1d-deformatie analyse uit waterpasnetwerken," Delft Univ. Technol., LGR Series, Delft, Netherlands, Tech. Rep. 5, 1994.
[21] P. J. G. Teunissen, D. G. Simons, and C. C. J. M. Tiberius, *Probability and Observation Theory*. Delft, The Netherlands: Delft Inst. Earth Observ. Space Syst., Delft Univ. Technol., 2005.
[22] J. J. van Zyl, "The Shuttle Radar Topography Mission (SRTM): A breakthrough in remote sensing of topography," *Acta Astronautica*, vol. 48, no. 5, pp. 559–565, 2001.
[23] G. Ketelaar, L. Zeijlmaker, and R. Hanssen, "Monitoring subsidence due to gas extraction using satellite radar interferometry in Groningen, the Netherlands," *Shell EP J. Technol.*, vol. 7004, pp. 35–38, Sep. 2006.
[24] M. Caro Cuenca, A. J. Hooper, and R. F. Hanssen, "Surface deformation induced by water influx in the abandoned coal mines in Limburg, the Netherlands observed by satellite radar interferometry," *J. Appl. Geophys.*, vol. 88, pp. 1–11, 2013.

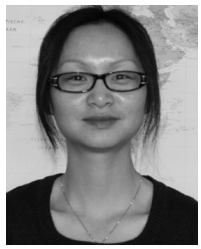

Ling Chang received the M.S.E. degree in geodesy and survey engineering from Tongji University, Shanghai, China, and the Ph.D. degree from the Delft University of Technology, Delft, The Netherlands, in 2010 and 2015, respectively.

She is currently a Postdoctoral Researcher working on structural health monitoring of railway infrastructure with the Department of Structural Engineering, Delft University of Technology. Her current research interests include statistical hypothesis testing, time-series modeling, and change detection, using satellite-borne remote sensing technology, with a focus on rail and infrastructure monitoring.

Rolf P. B. J. Dollevoet received the M.Sc. degree in mechanical engineering from the Eindhoven University of Technology, Eindhoven, The Netherlands, and the Ph.D. degree from the University of Twente, Enschede, the Netherlands, in 2001 and 2010, respectively.

Since 2003, he has been with ProRail, Utrecht, The Netherlands. Since 2012, he has been appointed as a part-time Professor with the Section of Road and Railway Engineering, Delft University of Technology, Delft, The Netherlands. He is also currently the Leader of scientific research on rolling contact fatigue and wheel-rail interface within ProRail Civil Engineering and the Chair of the International Union of Railways working group on wheel-rail conditioning and lubrication.

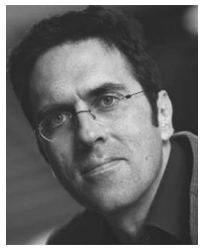

Ramon F. Hanssen (M'04–SM'15) received the M.Sc. degree in geodetic engineering and the Ph.D. (*cum laude*) degree from the Delft University of Technology, Delft, The Netherlands, in 1993 and 2001, respectively.

He was with the International Institute for Aerospace Survey and Earth Science (ITC), Stuttgart University; the German Aerospace Center (DLR); Stanford University (Fulbright Fellow); and the Scripps Institution of Oceanography, where he worked on microwave remote sensing, radar interferometry, signal processing, and geophysical application development. Since 2008, he has been an Antoni van Leeuwenhoek Professor in earth observation with the Delft University of Technology. He is the author of a textbook on radar interferometry.